Fibers and Polymers (2023) 24:4031–4047
https://doi.org/10.1007/s12221-023-00368-5

Online ISSN 1875-0052
Print ISSN 1229-9197

REGULAR ARTICLE

Evaluating the Reliability of Glass-Braid-Reinforced Polymer Composite Coil Spring for Automotive Suspension Development Using Finite Element Method and Empirical Tests

Jaeki Kwon[1] · Jungil Jeon[2] · Jungkyu Shin[2]

Received: 7 July 2023 / Revised: 6 September 2023 / Accepted: 12 September 2023 / Published online: 30 September 2023

Abstract
This study conducted a comprehensive assessment of the reliability of automobile glass-braid-reinforced polymer (GBRP) composite coil springs fabricated using a braiding technique. The evaluations encompassed durability, plastic deformation, and resistance to chipping, adhering to the industrial standards established for steel springs within the automobile industry. In addition, a method to evaluate the void distribution and impregnation rate is proposed to quantitatively evaluate the quality of the composite fabrication. A method for testing part of manufactured springs was developed using finite element analysis, and the validity of this testing method was confirmed through empirical testing. Upon completing the durability and plastic deformation examinations, the changes in the free height of the GBRP composite coil springs exceeded those of their steel counterparts by 47% and 162.5%, respectively. Notably, these tests revealed no discernible surface failures or fractures on the composite springs. To elucidate the changes in free height observed post-testing, scanning electron microscopy was employed to assess the incurred damage. Furthermore, results from the chipping resistance tests substantiated that the GBRP composite's safety attributes were not compromised by any surface damage.

Keywords Glass-braid-reinforced polymer (GBRP) · Durability test · Plastic deformation test · Chipping test · Damage evaluation · Finite element method (FEM)

1 Introduction

Research focused on optimizing the properties of components, including their weight, has become increasingly crucial. This urgency has stimulated research into the substitution of traditionally employed steel components with lighter and newer materials across various industries [1, 2]. In the automotive sector, efforts are being made to reduce the weight of drivetrain and chassis components through structural enhancements, the refinement of manufacturing methods, or the incorporation of lightweight and high-strength materials such as aluminum and magnesium [3]. Specifically, lightweight components can optimize the performance of vehicles by amplifying engine output and improving fuel efficiency. Therefore, the utilization of lightweight materials constitutes an effective and fitting strategy to prevent environmental pollution and conserve fuel [4]. Traditionally, non-ferrous metals such as aluminum alloys have been employed to diminish vehicle body weight; however, there is an emergent trend toward replacing these alloys with polymer composites, notably fiber-reinforced plastics [2, 5].

A fiber-reinforced polymer (FRP) is a composite material made of a polymer that's reinforced with fibers. These composites boast excellent mechanical properties, attributable to a matrix that shapes, confines, and effectively transmits stress to the fibers [6]. Moreover, fiber-reinforced composites display anisotropic behavior dependent upon the orientation of the fibers, a feature that can be altered to adjust their mechanical strength or stiffness [7]. Glass fibers are particularly beneficial due to their high mechanical strength, rigidity, and cost-efficiency [8]. Epoxy resins, a distinct category of polymers known for their strong adhesion, chemical resilience, corrosion resistance, thermal stability, excellent processability, and dimensional stability during manufacturing.

✉ Jungkyu Shin
comshin@youngwire.com

[1] R&D Team, Steel Division, Youngwire, Boryeong 33448, Korea

[2] R&D Center, Automotive Division, Youngwire, Boryeong 33448, Korea

These polymers can satisfy diverse requirements through the selective blending of various resins and curing agents [9]. Glass-fiber-reinforced plastics (GFRPs), particularly those incorporating epoxy resins, have ascended as a preferred material in polymer matrix composites [9].

The mechanical properties of these composite materials can be modified by adjusting the fiber alignment [10]. The braiding method can produce a preform with a multiaxial fiber structure by crossing two or more yarn types at an oblique angle to form a net-like structure. This method also facilitates the fabrication of intricate geometries with variable curvatures [11]. Notably, braided structures, which diverge from woven or knitted fabrics in their formation mechanisms, exhibit superb physical attributes such as elevated toughness, fatigue resistance, and impact resilience [12].

Extensive research has been conducted to explore the utility of braided composites. For instance, Pedro et al. scrutinized both material mechanics and the results of manufacturing trials to appraise the applicability of braided composites in commercial fuselage structures [13]. Li et al. manufactured 2D biaxially braided composites using a range of fiber materials and examined their tensile attributes and fracture behaviors at various temperatures using tensile testing and high-definition charge-coupled device optical microscopy [14]. Liu et al. investigated the longitudinal and transverse shear properties of 3D braided hybrid composites designed for aviation engine fan blades, focusing on the influence of hybridization and structural parameters [15]. Nega et al. conducted both experimental and numerical assessments of the buckling behavior exhibited by asymmetrically open-sectioned, triaxially braided circular arches when subjected to three-point bending [16]. Dorival et al. performed dynamic crush tests on a variety of composite structure designs pertinent to diverse aircraft components, including rotor blades, wing elements, and fuselages, to elucidate their energy absorption mechanisms [17].

While both analytical and experimental inquiries into the suitability of braided composites for aircraft components have been undertaken, their incorporation into automotive components, especially in the manufacture of suspension coil springs, is limited. Several researchers have studied the properties of coil springs constructed from composite materials. For example, Sequeira et al. employed finite element analysis to compare the attributes of composite and steel-based coil springs under different loading conditions [18]. Oh et al. utilized both numerical analyses and empirical methods to formulate a procedure for establishing the design parameters of composite coil springs [19]. Chen et al. examined the torsional attributes of polymer matrix composite spring wire rods (PMCRs) along with the compressive and resilient properties of polymer matrix composite helical springs (PMCHSs) [20].

Automotive coil springs typically experience alternating tensile and compressive stresses during vehicle operation, serving to mitigate shocks and vibrations. They also endure corrosive environments and sustain various forms of damage, such as chipping, over extended periods [21–23]. Consequently, the commercial introduction of composite coil springs necessitates comprehensive research and development (R&D) efforts from diverse vantage points. Among these, safety research focusing on the dynamic behavior of the springs remains a critical yet unexplored domain.

This motivated our study, which concentrated on automobile suspension coil springs. We manufactured a GBRP composite coil spring by braiding glass fibers and subsequently conducted practical tests to evaluate characteristics such as durability, plastic deformation, and chipping under long-term operating conditions. Such tests are commonplace in the automotive industry, though their results remain largely unpublished. Additionally, we analyzed the void distribution and impregnation rate to evaluate the quality of composite material production. The load–displacement behavior and free height change of each sample were evaluated before and after testing. Moreover, any damage potentially causing structural failure needs to be evaluated to ensure safety [24]. The damaged area of an advanced material that serves the intended use and reflects the design should also be appraised [24]. After mechanical testing, each sample underwent a visual inspection using scanning electron microscopy (SEM) to assess the damage, followed by an analysis of the factors influencing the change in free height. The results, procured through various methods to evaluate the reliability of automotive suspension coil springs manufactured using the braiding method with glass fibers, offer valuable insights for future reliability assessments of automotive composite parts under prolonged driving conditions.

2 Material and Methods

2.1 GBRP Composite Materials

The braid-reinforced composite coil spring used in this study was fabricated by employing glass yarn (1200Tex) as the reinforcing material and a blend of epoxy resin (KFR-120 V) and hardener (KFH-9584) as the base material. Given that the spring's shape was maintained through the epoxy and resin interaction, the optimal curing temperature and resin mixing ratio were experimentally determined. The preforms were produced using 16, 36, and 48 carriers wire braiding equipment with a braiding angle of 45° (Fig. 1).

Based on earlier reports, axial yarns can be introduced during manufacturing to enhance axial strength during braiding [25], and composite springs with a rubber core can augment the failure load during compression [26]. In

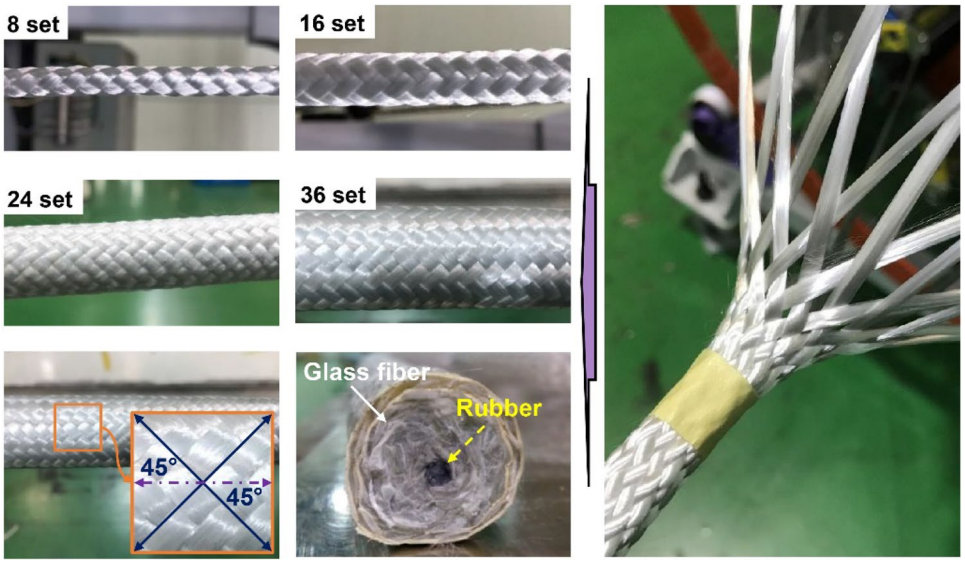

Fig. 1 Photographs showing the braiding process

this study, the cross-sectional center of the braid-reinforced composite coil spring consisted of a cylindrical rubber cross-section, and was fabricated by laminating layers comprising glass fibers from the core outward.

2.2 Manufacture of GBRP Composite Preform

The pre-impregnated (pre-preg) glass-braid-reinforced composite was processed into a semi-hardened state by mixing the epoxy resin and glass fiber as the base material. The GBRP composite coil spring used in this study was the ninth prototype created. The structure was manufactured using 36 braiding carriers and 19 layers and was guided by the production and evaluation results of the first eight prototypes [27–30]. The preform was cut to a 2.0 m length, taking into account the total length of the coil spring, and a peel ply, serving as a release agent, was applied to the preform's surface. The mesh was wound, excluding the resin injection and vacuum lines. Further, a vacuum bag was used to completely enclose the preform, and the vacuum condition was verified using connecting lines. The epoxy and curing agent's mixing ratio was set at 100:115, and the resin was injected into the preform by applying a vacuum pressure of 100 kPa at 40 °C (Fig. 2). This process required approximately 14 h to completely inject the resin into the preform.

As depicted in Fig. 3a, after the resin injection, the preform was wound around the mold core, and the remaining mold-fastening components were mounted. In this study, curing, which involves heating a thermosetting resin with glass fibers, was conducted twice to fully cure the resin. During the initial curing step, as shown in Fig. 3b, the fastened mold was placed in a hot-air oven and maintained at a

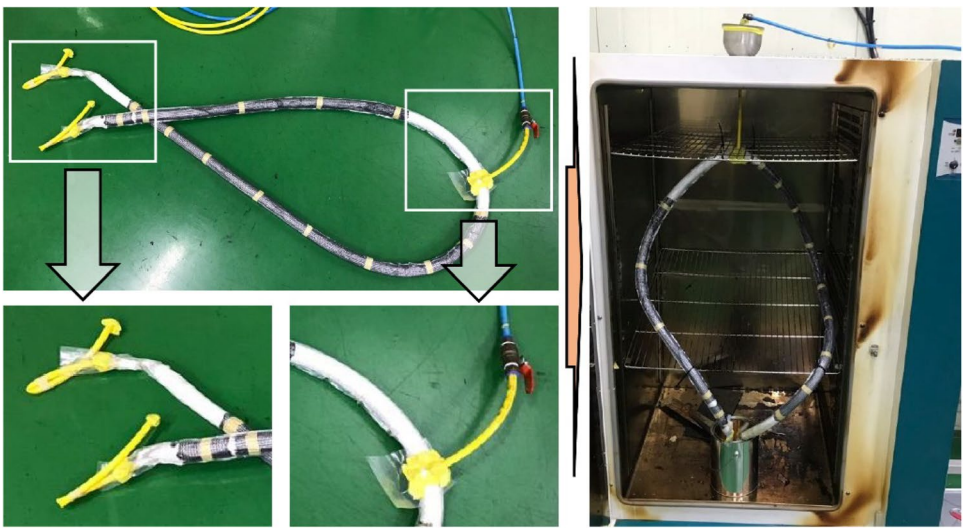

Fig. 2 Photographs of the process of resin injection into the preform

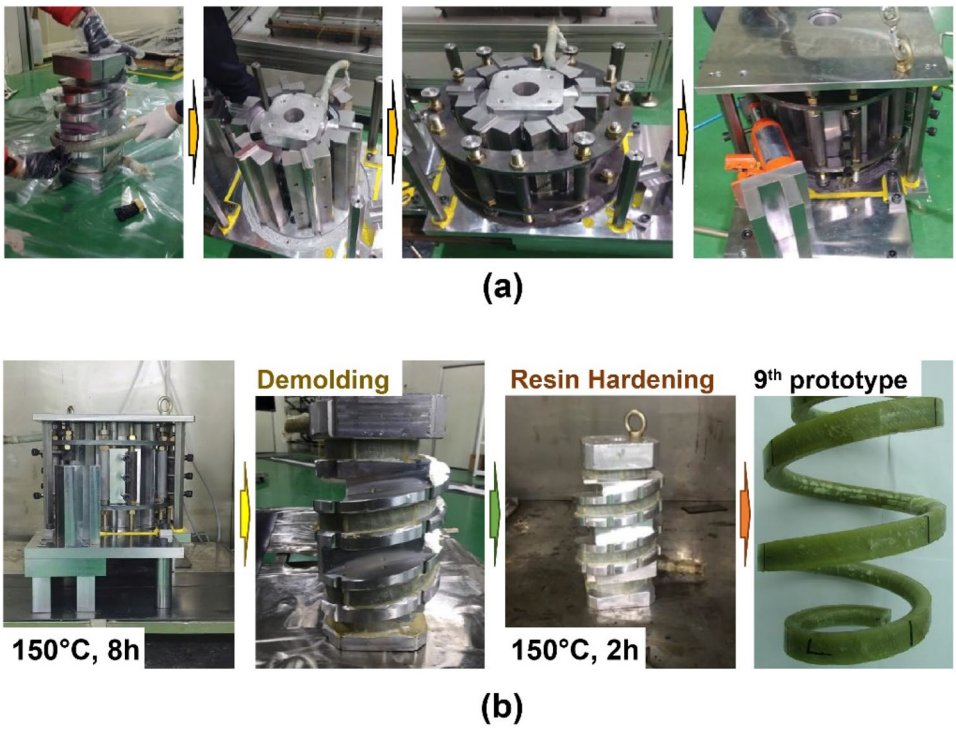

Fig. 3 Photographic images of the **a** mounting and **b** heating process for manufacturing the GBRP composite coil spring

molding temperature of 150 °C for 8 h. In the second curing step, the core metal mold was demolded and cured at 150 °C for another 2 h.

Compression molding was utilized for resin impregnation and pore removal. Notably, the part where the outer mold enveloped the preform was designed as a flat surface to effectively apply high pressure to the preform wound around the mold core during mold production. Additionally, the compression coil spring's stress is mechanically concentrated within the spring [31]. To lessen the weight of the spring, the exterior surface, which experiences relatively low stress, was flattened, while the inner surface was designed to resemble the shape of a general coil spring. Images of the cross-section and longitudinal section of the manufactured ninth prototype are shown in Fig. 4, indicating that the coil is "D"-shaped rather than circular. The interior of the spring exhibits a circular geometry, similar to that of a conventional coil spring, whereas the exterior portion is characterized by a flat profile. This approach resulted in a composite sample with no visible layers of resin or voids. The specifications of the ninth prototype are summarized in Table 1. The weight of the manufactured GBRP composite coil spring was found to be approximately 30% lower compared to that of iron-based materials.

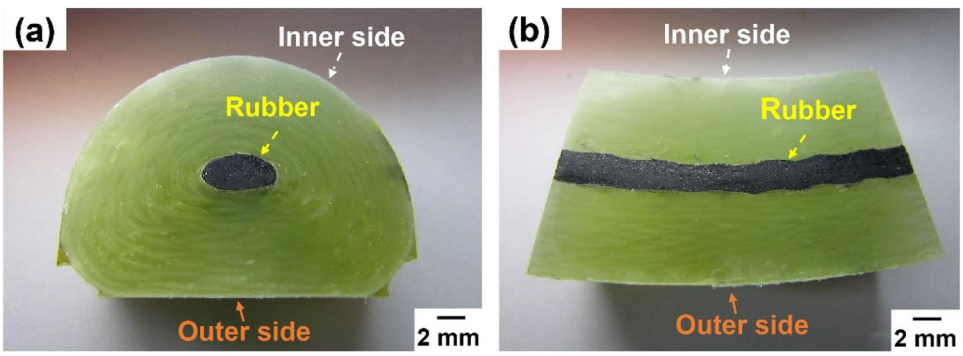

Fig. 4 Photographic images of the **a** cross-section and **b** longitudinal section of the coil spring composed of GBRP

Table 1 Design specifications for theoretical design and composition of the coil spring

	Theoretical design	Prototype 9th
Spring material	GBRP	GBRP
Molds	–	Metal
Weaving method	Braiding	Braiding
Test free height (mm)	303.4	300.1
Wire dimeter (mm)	25.5	22.5–23.5
Inner diameter (upper/lower, mm)	92.5/97.0	92.2/92.7
Outer diameter (mm)	192.2	179.6
Total spring coils	3.75	3.71
Weight (g)	1,515	1,401
Number of layers	22	19

3 Determination of Parameters for FEM

3.1 Measurement of Void Distribution and Impregnation Rate

To establish standards for evaluating the manufacturing quality of composite materials produced from braided preforms, cross-sectional samples were obtained from the ninth prototype before testing. The void distribution and maximum void area were measured using SEM, and the rate of void impregnation was evaluated. The direction crossing the core from one side of the spring to the other is designated as the tensile line (TL), while the direction from the inner or outer side of the spring, crossing the core to the opposite surface, is designated as the compression line (CL). All voids observable in the TL and CL of each sample at SEM × 40 magnification were targeted when measuring the void area.

3.2 Modeling and Boundary Conditions for Finite Element Method (FEM)

The durability of the automotive suspension coil springs was tested by applying pull-rebound and full-bump conditions for the maximum/minimum compression displacement. However, mechanical testing of the first eight prototypes of the GBRP composite coil spring indicated that dynamic characteristics, such as fatigue strength, were lower compared to static characteristics, like compressive strength, making the durability test standard challenging to implement [27–30]. Additionally, research data on the durability characteristics of fiber-reinforced composite coil springs were not available; therefore, this analysis focuses on predicting the displacement range of the spring that would not rupture the ninth prototype during its durability test. Generally, fatigue strength accounts for 35–60% of the tensile strength [32], and a displacement value corresponding to 50% of 24 kg_f/mm^2 [27], the breaking strength of the eighth prototype, was considered as the maximum compression displacement. As depicted in Fig. 5, a jig for spring compression and a coil spring with a total of 2.2 turns were modeled and assembled to simulate the state in which the coil spring was mounted on the jig.

For the static deformation analysis, we used Abaqus v6.14, a finite element method (FEM) program, to construct a model with 88,770 octahedral elements and 46,565 nodes. This model aimed to confirm the stress generated in the coil spring during maximum/minimum compression. As the FEM involves nonlinear static analysis, the contact conditions between the upper/lower jig and spring were specified, and the coil spring was permitted to undergo significant deformation. The jig was considered to consist of structural steel and the data of this material were used for the FEM. The data for the GBRP composite material used in the analysis was obtained from experiments. The material properties values used for the FEM are listed in Table 2. The applied compression displacement, which equaled the spring's height in the rebound stage, was 23.0 mm. For the boundary condition, a displacement was applied to the lower jig from the rebound stage with the composite coil spring mounted on the jig. Additionally, rotation along the z-axis was allowed during compression. The Contact Condition

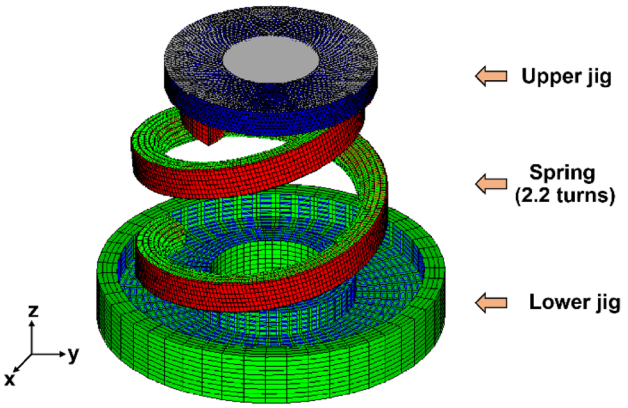

Fig. 5 Model constructed for FEM, showing the jig for spring compression and a coil spring with a total of 2.2 turns

Table 2 Material properties for FEM

Parts	Material	Young's modulus (MPa)	Poisson's ratio
Jig	Steel	2.0×10^5	0.3
Spring	GBRP	(4.4×10^4)	(0.28)

(): Property values of the spring are optimized and calculated through FEM to meet the criteria set by the compression test, under the assumption that the composite coil spring prototype behaves as an isotropic material

was set to General Contact, and the Contact Property was defined as Tangential Behavior with a friction factor of 0.1 and Normal Behavior with Hard Contact. The suspension system was equipped with a spring.

3.3 Mechanical Property Tests

In the automotive industry, a vertical load is applied to the suspension coil spring while the vehicle is in motion [33]. Since vibrations in a vehicle are typically generated perpendicular to the road surface, we simulated driving conditions using a compression tester. Given the high cost of manufacturing composite springs, we cut the ninth prototype into two springs for testing. We isolated only one active turn in the coil spring for examination [34]. However, a typical coil spring is made up of inactive and active turns [35], with at least two turns preferred due to differing stress behaviors across parts. Hence, we took samples equivalent to two turns from the ninth prototype for durability, plastic deformation, and chipping tests, given the limited number of composite springs.

We conducted the durability test (Fig. 6a) for up to 4.15×10^5 cycles at a frequency of 1.2 Hz using a dynamic testing machine at room temperature. We based the values for the displacement range and stress ratio on the finite element analysis. We added 1.15×10^5 cycles to the initially set condition of 3.0×10^5 cycles to simultaneously conduct the durability and plastic deformation tests, and to compare the damage state.

The plastic deformation test (Fig. 6b) took place in a hot-air circulating oven. We secured a spring to the jig and maintained the height corresponding to the loading load for 96 h at 80 °C.

We performed the chipping test (Fig. 6c) using chipping test equipment. After securing the spring to the equipment, we kept it at − 40 °C for more than 4 h. During the test, we applied pressure of 480 kPa to gravel particles ranging from 8.0 to 16.0 mm in size. We rotated the spring's surface around the vertical axis for 20 s and then released it.

Furthermore, we measured and analyzed the load–displacement behavior and change in the free height of each sample before and after the tests to evaluate the long-term operational reliability of the GBRP composite coil spring. We conducted the test using Zwick/Roell Z020 equipment, applying a compressive load at room temperature with a displacement control of 10.0 mm/s. We visually inspected the tested samples' surfaces to evaluate the damage and confirm the presence and distribution of cracks. In addition, we collected cross-sectional samples from the top, middle, and bottom zero turns of each spring. We polished the cross-sections with sandpaper #1200 and #2000, and used SEM to analyze the crack initiation, propagation behavior, and failure mode.

4 Results and Discussion

4.1 Analysis of Void Distribution and Impregnation of GBRP Composite Coil Springs

Figure 7 presents the results of the void distribution and impregnation rate analysis of a composite coil spring. In the cross-sectional sample of the ninth prototype, voids measured along the TL were distributed from the surface to the core, with the area adjacent to the core containing the maximum number of voids, measuring 109,630 μm^2 (Fig. 7a). Most voids along the CL were found across the area adjacent to the central fiber layer, albeit in fewer numbers than along the TL. However, the area with the most voids on the CL was next to the inner side of the spring, measuring 23,389 μm^2 (Fig. 7b). Moreover, based on the core, the voids measured from the outer surface of the spring to the core were about 2.5 times more numerous than those measured from the inner surface to the core.

Table 3 lists the total area, total void area, and void impregnation rate of the cross-sectional samples, excluding the rubber core. The TL and CL void impregnation rates were 99.3% and 99.8%, respectively, indicating a slightly higher rate along the CL. This discrepancy in void impregnation rate could be attributed to the reduction of voids inside the composite material, which occurs when the resin inside the preform escapes due to the force applied along the CL during mold fastening. Previous studies have shown that voids within braid-reinforced composites can act as potential defects, significantly contributing to the deterioration of mechanical properties such as interlaminar shear characteristics and interlaminar fracture toughness, both heavily influenced by the resin [36]. Additionally, the void impregnation rate is a critical determinant of the quality of braid-reinforced composites, with the degree of mechanical property degradation increasing with the number of voids [37–39]. The difference in the void impregnation rate between the TL and CL for the ninth prototype manufactured in this study was 0.5% *p*, reaching 99.6% when calculated based on the sample and core area. This rate is 1.2% *p* higher than that of the eighth prototype produced in a previous study [27].

4.2 FEM Results to Confirm the Safety of the Conditions Applied to the Durability Test

The spring experienced maximum stress on the inside of the 2.0 turns, with the lower part possessing a broader spring radius, exhibiting more stress than the upper part with a narrower spring radius. Additionally, the stress was relatively low at the outer edge and adjacent sections

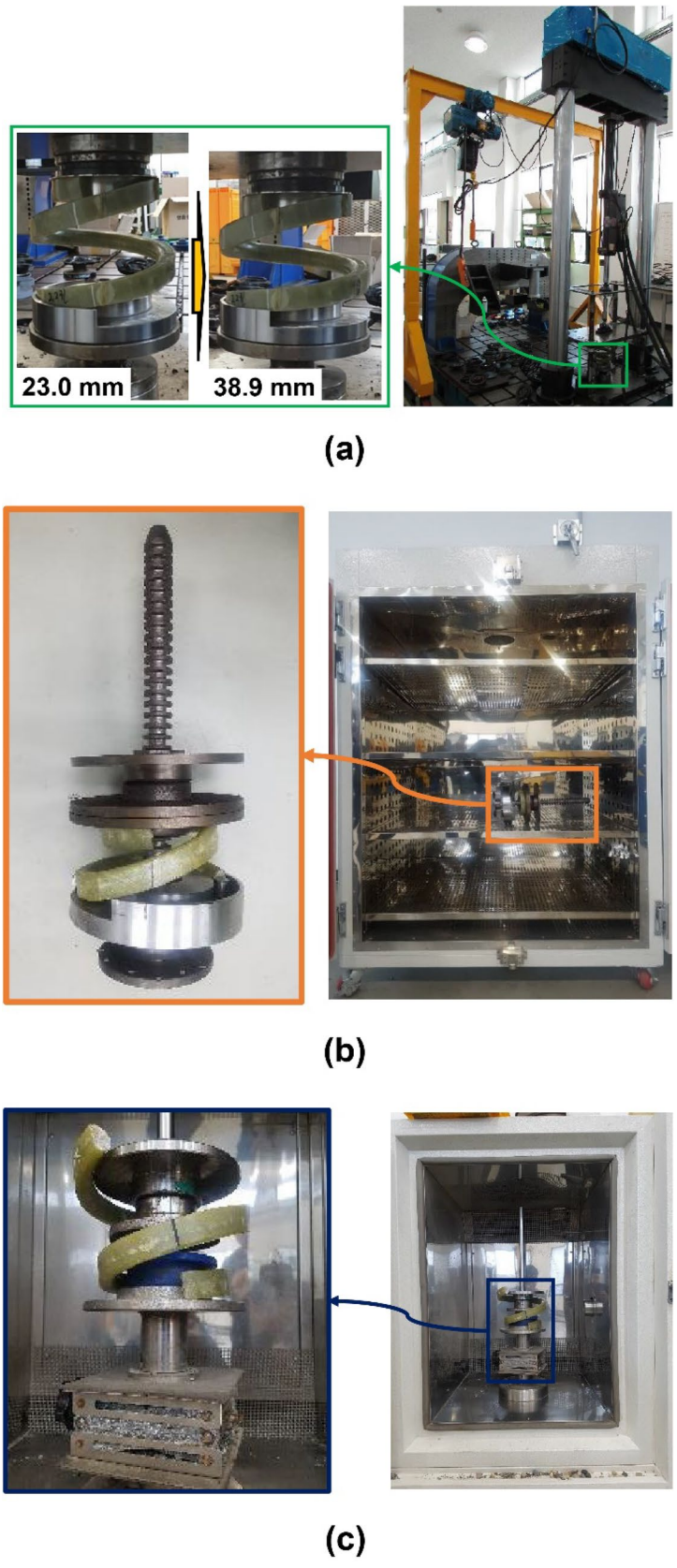

Fig. 6 Photographs of equipment for **a** durability, **b** plastic deformation, and **c** chipping tests

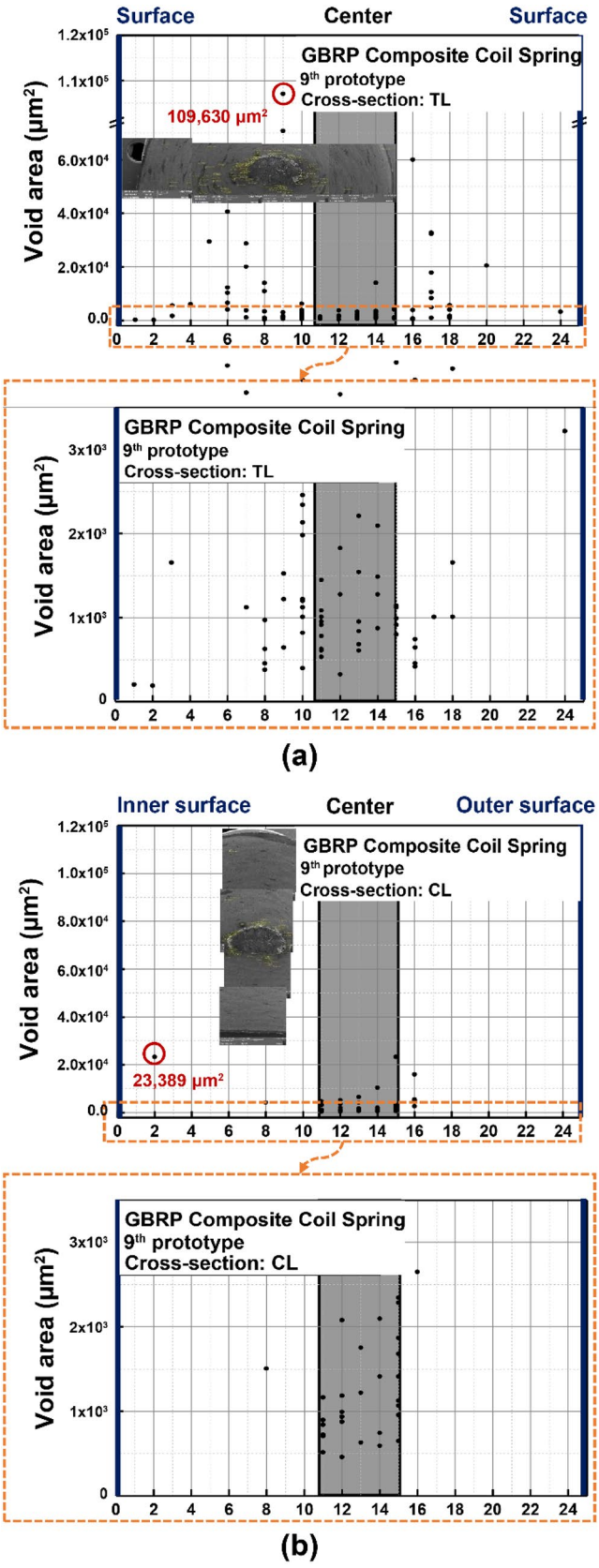

Fig. 7 Plots representing the void distribution along the **a** tensile and **b** compression lines of cross-sectional specimens of the GBRP composite

Table 3 Impregnation rate data for the TL and CL of the GBRP composite cross-sectional specimens

Observation direction	Total area–core area (μm^2, A)	Total void area (μm^2, B)	Void impregnation rate $\{(A - B)/A\}$	Total impregnation rate (%)
TL	95,153,261	704,702	0.993	99.6
CL	101,786,606	161,493	0.998	

of the spring. Figure 8a illustrates the stress distribution in the fully bound state. The spring experienced a tilt at a compression displacement of 23.0 mm, but remained stable. The maximum stress inside the spring was computed to be 6.6 kg_f/mm^2. This value was considered the minimum stress that the spring would encounter during the endurance test. The stress distribution at a compressive displacement of 95.8 mm is shown in Fig. 8b. The maximum spring stress was 31.2 kg_f/mm^2, with a slight spring inclination observed. At a compression displacement of 108.9 mm (Fig. 8c), the maximum spring stress was 36.3 kg_f/mm^2. Considering the contact between the spring wire diameters, premature failure might occur during the durability test. The stress–displacement graph calculated using FEM is shown in Fig. 9. From the fully bound state to the displacement condition where contact between the spring wire diameters might occur, the results were calculated as a linear function. The displacement corresponding to 50% of 24.0 kg_f/mm^2 (the breaking stress of the eighth prototype) was predicted to be 38.9 mm. The FEM results corresponding to a compression displacement of 38.9 mm are shown in Fig. 8d. The maximum internal spring stress was 12 kg_f/mm^2, and this predicted displacement was chosen as the durability test condition. Therefore, the FEM determined the maximum and minimum displacements applied to the spring during the durability test to be 38.9 mm and 23.0 mm respectively, resulting in an R-ratio ($\sigma_{min}/\sigma_{max}$) of 0.55.

4.3 Long-Term Durability Evaluation of the GBRP Coil Spring

During the durability test, no failures were observed in the spring, and no surface cracks were found after test completion. The load–displacement curves of the composite samples before and after the durability test are displayed in Fig. 10a. Based on the initial load applied at the test's conclusion, displacement exhibited a linear increase in relation to the load, with each slope evaluated similarly. However, the free height was reduced by 5.88 mm after the test, compared to before the durability test. For steel springs, the free height change before and after the durability test typically falls within 4.0 mm on average. Based on these trends, the durability of the GBRP composite coil spring produced in this study surpassed that of the steel spring by 47%. No failures or cracks were observed in the samples after the plastic deformation test.

The load–displacement curves, as shown in Fig. 10b, reveal that the slopes of the curves before and after the test were similar. However, a change in the slope was observed within the same load range. No damage to the spring was detected during the load test, suggesting that the observed change in tilt could be due to interference between the spring and the jig. Moreover, the free height of the spring decreased by 10.5 mm after the test compared to before the plastic deformation test, surpassing the result of the steel spring by 162.5%.

When a steel-made coil spring undergoes prolonged application of a constant load, plastic deformation may occur even within the material's elastic limit [40]. This phenomenon resembles creep, which notably occurs at higher temperatures. Still, in the case of a spring with significant design stress, it may occur even at room temperature [40]. As the applied load or load deformation increases, the spring's dimensions may change, and its mechanical characteristics may deteriorate [40]. However, the failure modes of GBRP composites differ from those of ferrous materials. The failure modes of composites can be categorized into fiber, matrix, and delamination failures [41, 42]. Furthermore, the discontinuous part appearing in the load–displacement curve during loading is known as the pop-in phenomenon [43]. Breakage may occur in fiber bundles within the composite material's matrix [44].

Load tests were conducted using samples before and after each test. Based on similarly evaluated slopes, fiber failure and matrix failure may occur during the durability and plastic deformation tests, thereby impacting the free height of the composite coil spring. Further, the changes in the free height observed after the durability and plastic deformation tests indicate that the plastic deformation test conditions caused more significant damage to the GBRP composite coil spring.

Figure 11 displays photographs of the damaged surface areas and the sample post-chipping test. When gravel was dialyzed, the material failed to absorb the impact energy, leading to surface flaws. Previous reports suggest that the structural properties of braid-reinforced composites rapidly deteriorate when damage occurs due to an object's impact [45, 46]. Nevertheless, the load–displacement curves obtained using the samples before and after the chipping test demonstrated the same trend (Fig. 10c).

4.4 Damage Evaluation

The relationship between the change in free height and the failure behavior of GBRP composite coil springs after

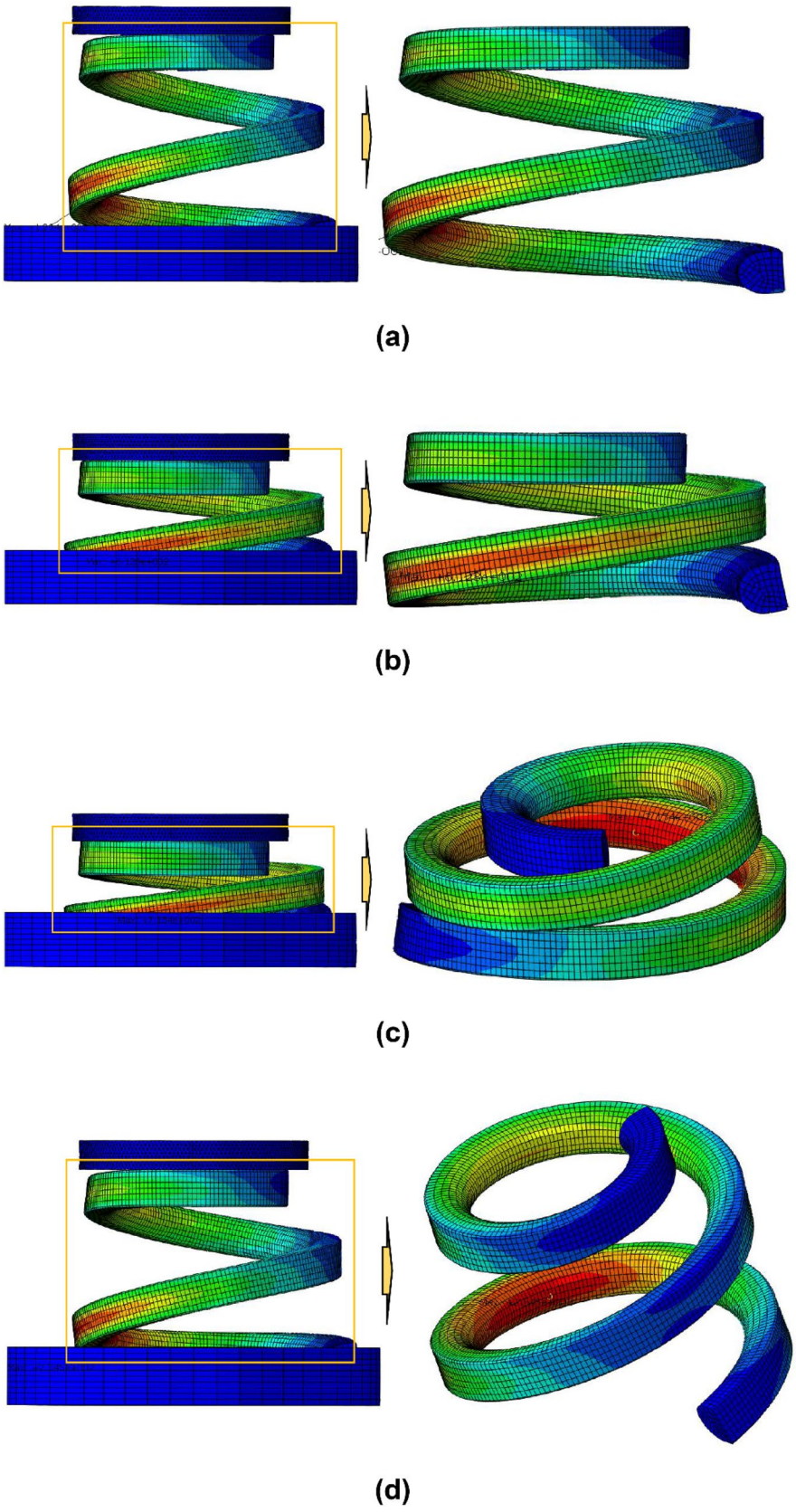

Fig. 8 Stress distribution and maximum stress analysis results when displacements of **a** 23, **b** 95.8, **c** 109.8, and **d** 38.6 mm were applied to the coil springs

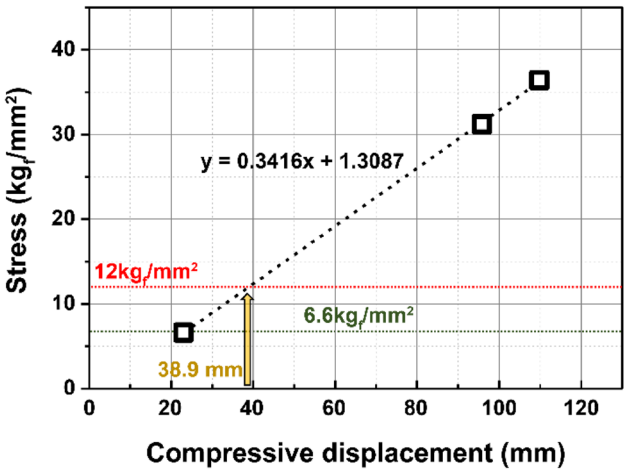

Fig. 9 Displacement as a function of applied stress to coil spring calculated using finite element method

the durability and plastic deformation tests was evaluated using SEM. The results are shown in Fig. 12. Figure 12a shows low- and high-magnification SEM images of the cross-sectional samples taken from the half-coil, two-coil, and four-coil portions of the spring after the durability test. The arrows in images (α) to (γ) indicate areas where cracks were confirmed at low magnification. Examining the spring's interior, where the stress was concentrated during the test, revealed failure modes such as cracks at the interface between the fibers and resin, fiber failure, and matrix failure. The phenomenon of stress concentration inside the spring upon application of a compressive load was confirmed using FEM. However, SEM observation of the cross-sectional samples revealed that the cracks were more densely distributed from the core to the edge compared to the inner part of the spring. The corner corresponds to the spring's outer part, and during manufacturing, the preform is pressed; thus, the glass fibers are densely packed. Consequently, the resistance to crack initiation and propagation was reduced because the area occupied by the matrix was significantly smaller than that of the other areas.

Figure 12b shows SEM images of cross-sectional samples taken from the upper zero turn and the middle and lower zero turns of the spring after the plastic deformation test. The behavior of crack initiation and the distribution of cracks in the inner part exhibited similar trends to those observed in the samples after the durability test. However, the damage tended to be more widespread. Delamination occurs when the load on the composite plies surpasses the interlaminar fracture toughness of the composite, leading to layer separation, interlaminar cracks, and discontinuities in the material [47]. In areas of high deformation, failure modes such as delamination failure were also observed.

Glass fiber, a reinforcing material, has a coefficient of thermal expansion close to zero [48]. However, resins may undergo strength degradation even at 60 °C [49]. Furthermore, the temperature and deformation conditions applied during the plastic deformation test accelerated crack initiation and propagation in the GBRP composite. The change in free height observed before and after both the durability and plastic deformation tests aligned with the results of the damage analysis using SEM. This explains the significantly large change in free height after the plastic deformation test compared to that after the durability test. Assuming uniform geometry and effective dispersion of glass fibers within the epoxy matrix, the prevalent form of fatigue anticipated during the operational lifespan of braided glass/epoxy composites is likely to commence with crack initiation at the fiber-resin interface, subsequently leading to interlaminar delamination. This constitutes the primary failure mechanism in fiber-reinforced composites. Prior research has involved the fabrication of GBRP composite coil springs and bars, featuring varying fiber orientations, thicknesses, and weaving techniques. These specimens underwent damage analysis via static testing methodologies and SEM [27–30]. Although the extent of damage varied among the specimens, the modes of damage exhibited considerable consistency [27–30]. In this study, a similar pattern was noted during the assessment of damage for samples subjected to durability and plastic deformation tests.

To enhance the crack resistance of the composite spring, it is recommended to design it with a round shape and large radius corners where the density of the glass fiber increases excessively. Since delamination failure can directly influence the reduction of strength and safety of the composite, it is suggested that the glass fiber layer be manufactured with less stacking than currently applied. This can improve the adhesion of the glass fiber by increasing the distribution area of the resin.

SEM was utilized to inspect the damaged portion of the cross-sectional sample after the chipping test. This was done to analyze the depth and failure pattern of the defects observed on the sample surface, and the results are depicted in Fig. 13. Damage was observed only on certain parts of the uppermost surface layer of the spring, where fiber breakage and resin peeling occurred. The damage extended to depths of approximately 18–142 μm, and the cracks that developed in the transverse direction were approximately 181–252 μm below the surface of the damaged part. Kang et al. studied the impact resistance of filament-winding composites and reported that the fibers tended to break even at a certain distance from the impact point [50]. When impact damage occurs, local vibrations and load reduction transpire [51], and these physical phenomena may affect the sample's surface and adjacent areas. Furthermore, matrix damage, which is the initial form of composite material damage comprised

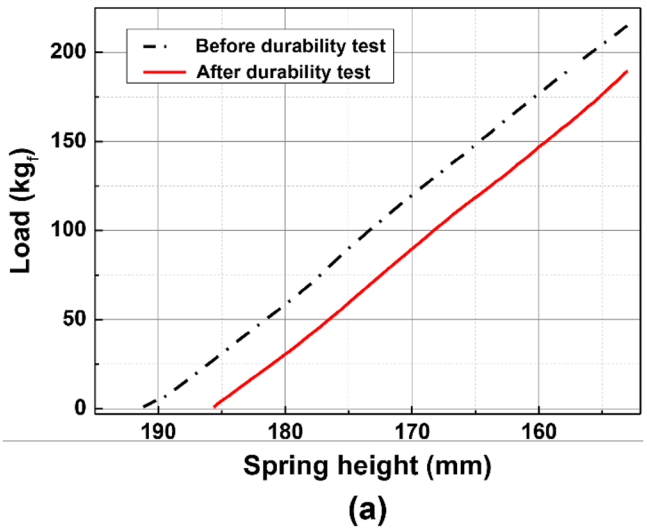

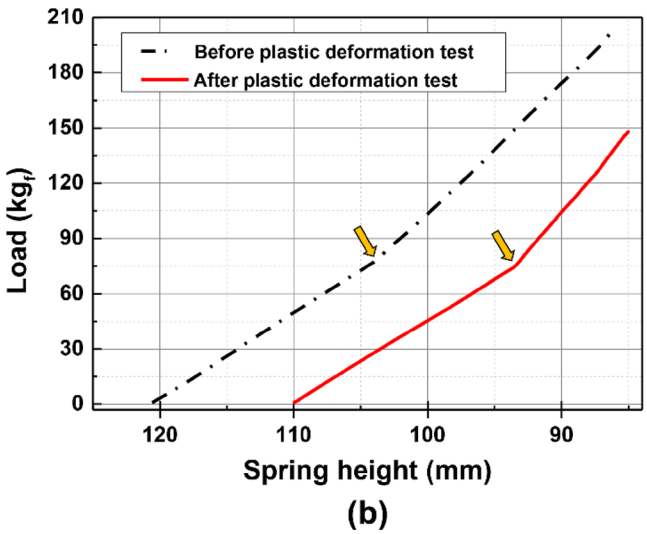

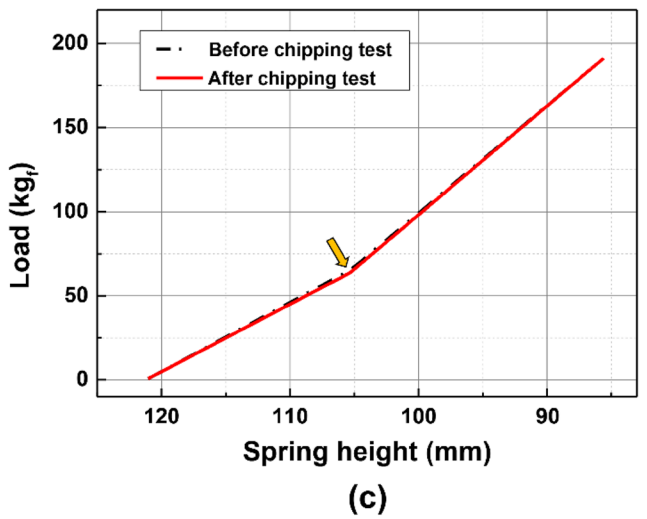

Fig. 10 Load–displacement of the GBRP composite coil spring before and after the **a** durability, **b** plastic deformation, and **c** chipping tests

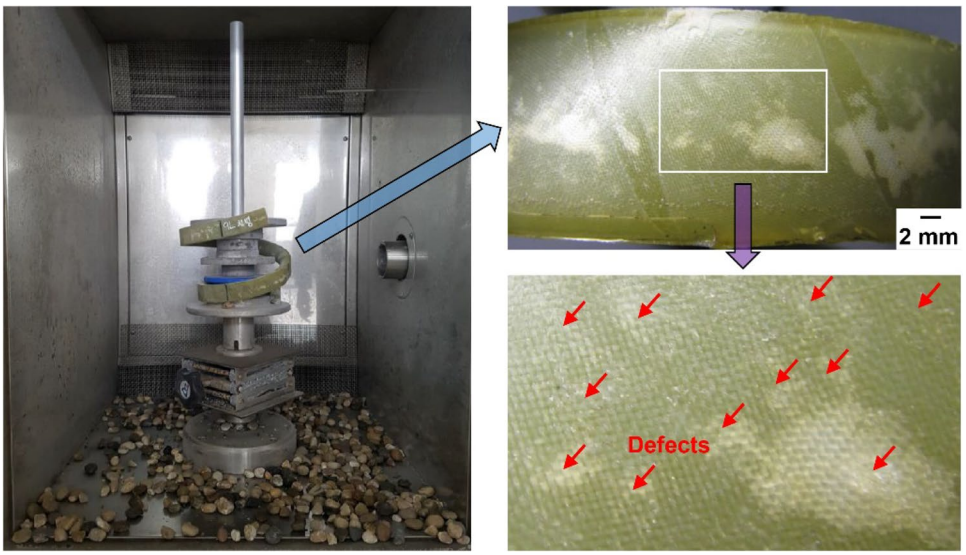

Fig. 11 Photographs of damaged parts on the surface of the GBRP composite coil spring after chipping test

of laminated structures, does not immediately lead to a final fracture. Instead, it reduces the structure's stiffness and causes separation between layers [52–54]. However, according to the load–displacement curve, the damage at a depth of approximately 250 μm caused by the impact applied to the sample surface during the chipping test had a negligible effect on the static properties of the structure.

5 Conclusions

In this study, we conducted practical durability, plastic deformation, and chipping tests to assess the reliability of GBRP composite coil springs, considering long-term usage conditions post-manufacturing. The conclusions were drawn based on the load and displacement behavior, change in free height, and damage evaluation.

1. Automotive suspension coil springs were fabricated using GBRP composites, and their reliability was assessed based on the testing methods applied to ferrous coil springs. Additionally, a method to quantitatively evaluate the manufacturing quality of the composite materials was proposed, focusing on the void distribution and impregnation rate. The impregnation rate of the manufactured spring was found to be 99.6%.
2. To reduce manufacturing costs, a method was established for testing a portion of the manufactured spring using finite element analysis. The validity of this testing method was confirmed through an actual test. Notably, the spring showed no damage after enduring 4.15×10^5 cycles at a stress range of 6.6–12.0 kg_f/mm^2, validating its durability.
3. After the durability and plastic deformation tests, the free heights of the GBRP composite coil springs exceeded those of the steel springs by approximately 47% and 162.5%, respectively. This difference in free height may stem from the low resistance to crack initiation and propagation at the fiber/resin interface, which is the primary failure mode of the composites. Moving forward, we plan to reassess the geometry and manufacturing methods to enhance the spring's performance.
4. Damage evaluation revealed that cracks were densely dispersed from the core to the edge in contrast to the spring's inner part where stress was primarily concentrated. There was a notable correlation between larger damaged areas and significant changes in free height. High-deformation areas exhibited failure modes such as delamination. For the optimization of future prototypes, it is suggested that corner rounding is implemented and the radius is increased. Furthermore, broadening the resin distribution area is suggested to mitigate the risk of delamination failure. This could be achieved by producing the glass fiber layer with fewer stacks than currently utilized. Post-chipping test observations revealed a damaged area with a depth ranging from approximately 18–142 μm on the spring surface. However, this damage seemed to have a negligible effect on the static properties of the GBRP composite.

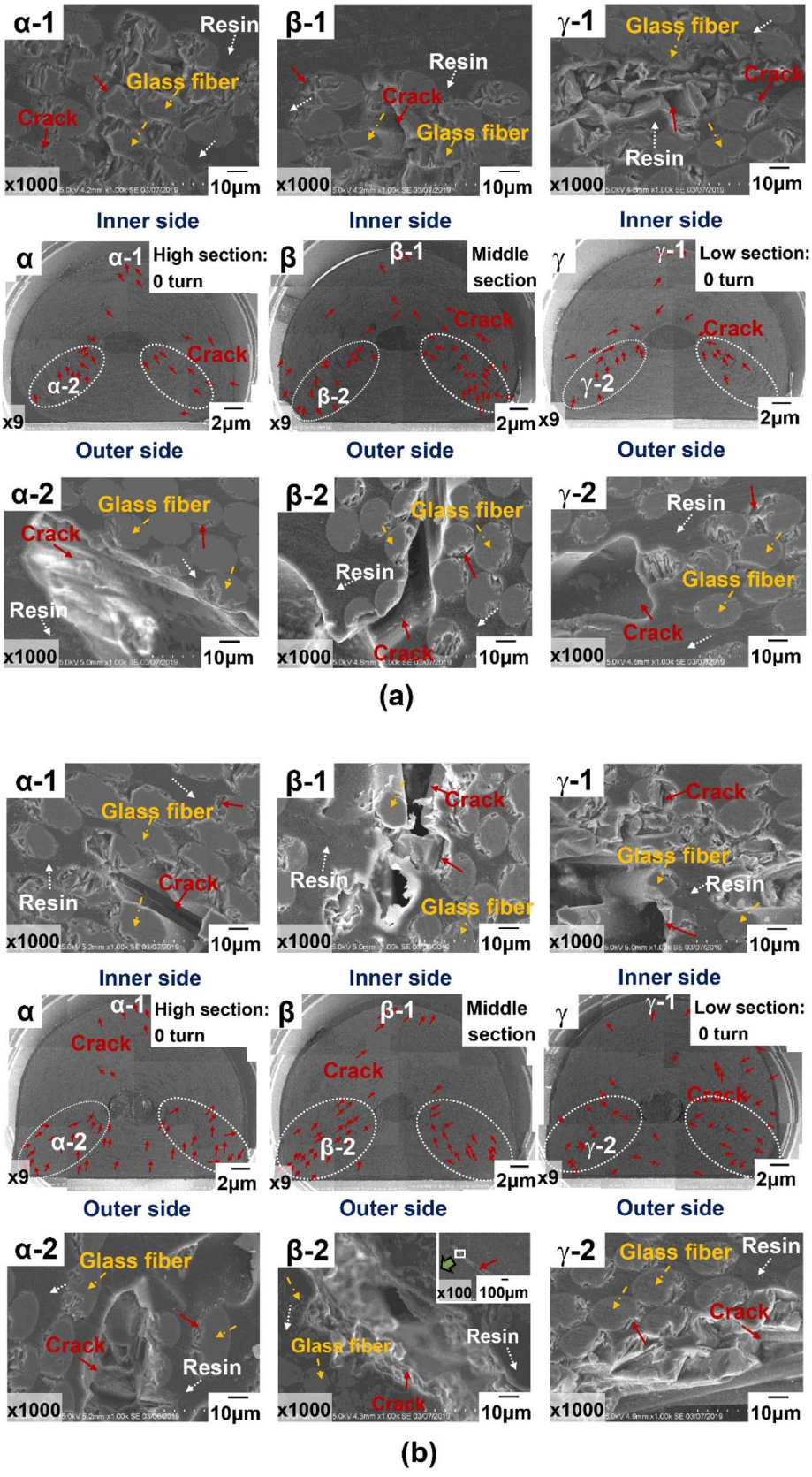

Fig. 12 Photographs of crack initiation, propagation, and distribution observed in the cross-sectional specimens taken from the upper 0, middle, and lower 0 turns of the GBRP composite coil springs after the **a** durability and **b** plastic deformation tests

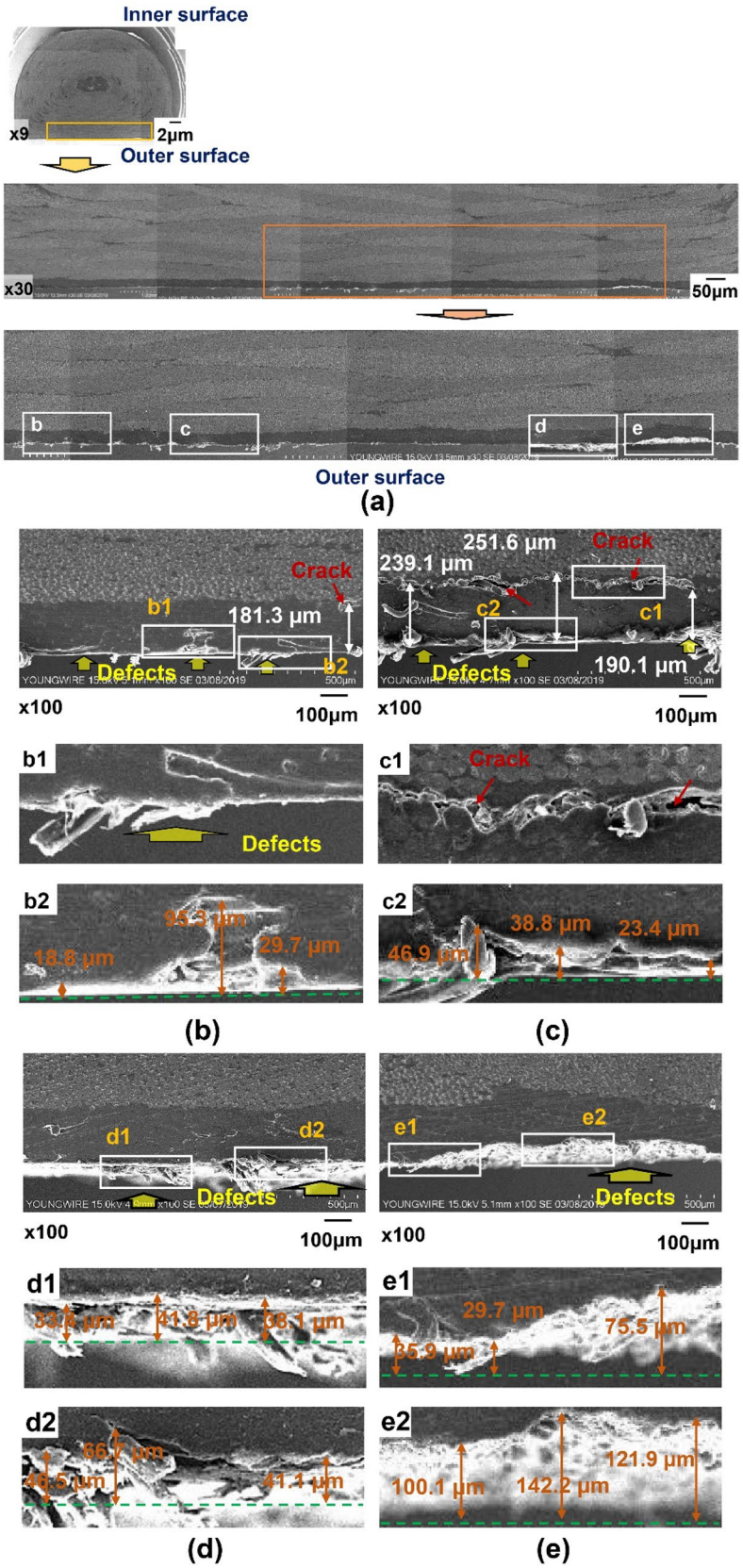

Fig. 13 Photographs of **b**–**e** damaged area and depth below **a** the outer surface of the GBRP composite cross-sectional specimen after the chipping test

Acknowledgements This research was conducted as part of Youngwire project titled "Development of high-durability composite coil springs."

Author Contributions JK led the conception and design of the study, carried out the experiments, analyzed the data, and drafted the manuscript, providing the key conceptual ideas and proof outline. JJ significantly contributed to the manuscript by reviewing and editing it, as well as analyzing the data. JS played a crucial role in designing and implementing the research, reviewing and editing the manuscript, and conducting the numerical analysis and experimentation.

Funding This work was supported by Hyundai Motor Company in 2018 and Youngwire in 2019.

Data Availability The datasets used and/or analyzed during the current study available from the corresponding author on reasonable request.

Declarations

Conflict of interest The authors declare that they have no known competing financial interests or personal relationships that could have appeared to influence the work reported in this paper.

Ethics approval Not applicable.

Consent Not applicable.

References

1. M. Choudhary, A. Sharma, M. Dwivedi, Fibers Polym. **20**, 823–831 (2019). https://doi.org/10.1007/s12221-019-8863-6
2. J.Y. Shim, M.W. Park, I.S. Kim, J. Weld. Join **41**(1), 37 (2023). https://doi.org/10.5781/JWJ.2023.41.1.4
3. W. Zhang, J. Xu, A review. Mater. Des. **221**, 110994 (2022). https://doi.org/10.1016/j.matdes.2022.110994
4. L.W. Cheah (2010), Thesis, Engineering Systems Division, Massachusetts Institute of Technology (MIT), USA.
5. H. Mohammadi, Z. Ahmad, S.A. Mazlan, M.A.F.J. Johari, G. Siebert, M. Petrů, S.S.R. Koloor, A. Review, Polymers **15**, 193 (2023). https://doi.org/10.3390/polym15010193
6. M. Kalova, S. Rusnakova, D. Krzikalla, J. Mesicek, R. Tomasek, A. Podeprelova, J. Rosicky, M. Pagac, Polymers **13**, 2949 (2021). https://doi.org/10.3390/polym13172949
7. S. Mortazavian, A. Fatemi, Compos. B **72**, 116 (2015). https://doi.org/10.1016/j.compositesb.2014.11.041
8. K.L. Pickering, M.G. Aruan Efendy, T.M. Le, Compos. Part A **83**, 98 (2016). https://doi.org/10.1016/j.compositesa.2015.08.038
9. L. Wang, J. Wang, Y. Qi, F. Zhang, Z. Weng, X. Jian, Polymers **10**, 708 (2018). https://doi.org/10.3390/polym10070708
10. Y. Zhuang, B. Zou, S. Ding, P. Wang, Coatings **12**, 1000 (2022). https://doi.org/10.3390/coatings12071000
11. H. Tan, L. Liu, Y. Guan, W. Chen, Z. Zhao, Compos. Struct. **209**, 317 (2019). https://doi.org/10.1016/j.compstruct.2018.10.102
12. P. Ma, Z. Gao, J. Ind. Text. **44**(4), 572 (2015). https://doi.org/10.1177/1528083713503001
13. M.J. Fedro, K. Willden, Ninth DOD(NASA)FAA Conf. Fibrous Compos. Struct. Des. **2**, 935 (1992)
14. Q. Li, Y. Gao, F. Ruan, Sci. Eng. Compos. Mater. **30**, 20220191 (2023). https://doi.org/10.1515/secm-2022-0191
15. L. Liu, G. Luo, W. Chen, Z. Zhao, X. Huang, Int. J. Aerosp. Eng. **2018**, 5906078 (2018). https://doi.org/10.1155/2018/5906078
16. B.F. Nega, K. Woo, H. Lee, Compos. Res. **32**(5), 249 (2019). https://doi.org/10.7234/composres.2019.32.5.249
17. O. Dorival, P. Navarro, S. Marguet, C. Petiot, M. Bermudez, D. Mesnagé, J.F. Ferrero, Compos. B **78**, 244–255 (2015). https://doi.org/10.1016/j.compositesb.2015.03.083
18. A.A. Sequeira, R.K. Singh, G.K. Shetti, J. Mech. Eng. Autom. **6**(5A), 63 (2016). https://doi.org/10.5923/c.jmea.201601.12
19. S.H. Oh, B.L. Choi, Trans. Korean Soc. Mech. Eng. A **38**(1), 31 (2014). https://doi.org/10.3795/KSME-A.2014.38.1.031
20. L. Chen, L. Wu, H. Fu, Y. Tang, Polymers **14**, 3900 (2022). https://doi.org/10.3390/polym14183900
21. H. Jagodang, H. Husaini, T.E. Putra, D. Schramm, Key Eng. Mater. **892**, 124 (2021). https://doi.org/10.4028/www.scientific.net/KEM.892.124
22. J.L. Porteiro, Thesis, Department of Mechanical Engineering, University of South Florida, USA (2010)
23. J.Z. He, J.N. Lu, X.Y. Deng, X.Q. Xing, Z.C. Luo, Results Eng. **16**, 100749 (2022). https://doi.org/10.1016/j.rineng.2022.100749
24. R. Jones, S.C. Galea, J.J. Paul, Aeronautical Research Labs Melbourne (Australia), Technical Report 23, AR-008-409 (1993).
25. J. Wang, P. Li, M. Wang, J. Sens. **2022**, 6358247 (2022). https://doi.org/10.1155/2022/6358247
26. C.H. Chiu, C.L. Hwan, H.S. Tsai, W.P. Lee, Compos. Struct. **77**, 331 (2007). https://doi.org/10.1016/j.compstruct.2005.07.022
27. J.K. Kwon, J.I. Jeon, J.K. Shin, Compos. Res. **35**(6), 435 (2022). https://doi.org/10.7234/composres.2022.35.6.439
28. J.K. Kwon, J.K. Shin, M.H. Kim, 2019 Spring Conf. Korean Soc. Compos. Mater., Yeosu, Korea; (2019), April 3–6.
29. J.K. Kwon, M.H. Kim, J.K. Shin, The 4th Inter. Conf. Active Mater. Soft Mechatr., Incheon, Korea, (2019) October 16–19.
30. J.K. Shin, Y.K. Goo, J.I. Jeon, J.K. Kim, K.H. Park, G.S. Yoo, S.J. Kim, 2019 Spring Conf. Korean Soc. Compos. Mater., Yeosu, Korea, (2019) April 3–6.
31. M.T. Todinov, Int. J. Mech. Sci. **41**, 357 (1999). https://doi.org/10.1016/S0020-7403(98)00068-X
32. F.C. Campbell, *Elements of metallurgy and engineering alloys* (ASM Technical Books, ASM International, 2008)
33. Y. Molev, D. Proshin, E. Stepanov, S. Maleev, I. Mavleev, I. Salakhov, IOP Conf. Ser. Mater. Sci. Eng. **695**, 012028 (2019). https://doi.org/10.1088/1757-899X/695/1/012028
34. M. Hük, S. Hoffmann, Technical Specification. SCTM-02 iABG 2013.
35. R.F. Vogt, M. Wis, Trans. Am. Soc. Mech. Eng. **56**(6), 467–476 (1934)
36. N. Han, O. Yuksel, J.S.M. Zanjani, L. An, R. Akkerman, I. Baran, Appl. Compos. Mater. **29**, 1061 (2022). https://doi.org/10.1007/s10443-021-10000-5
37. X. Liu, F. Chen, Eng. Trans. **64**(1), 33 (2016)
38. M. Mehdikhani, L. Gorbatikh, I. Verpoest, S.V. Lomov, J. Compos. Mater. **53**(12), 1579 (2019). https://doi.org/10.1177/0021998318772152
39. M.J. Hassan, A.R. Othman, S. Kamaruddin, Adv. Mater. Res. **795**, 64 (2013). https://doi.org/10.4028/www.scientific.net/AMR.795.64
40. A. Ramesh, Thesis, Mechanical Engineering (The University of North Carolina at Charlotte, USA 2009)
41. D.H. Kim, K.H. Jung, I.G. Lee, H.J. Kim, H.S. Kim, Compos. Struct. **176**, 757 (2017). https://doi.org/10.1016/j.compstruct.2017.06.031
42. J. Wang, L. Chen, W. Shen, L. Zhu, Polymers **14**, 2318 (2022). https://doi.org/10.3390/polym14122318
43. P. Kavouras, D.A. Dragatogiannis, D.I. Batsouli, C.A. Charitidis, Polym. Test. **61**, 197 (2017). https://doi.org/10.1016/j.polymertesting.2017.05.023
44. S. Kawazoe, Y. Kagawa, Sci. Technol. Adv. Mater. **2**, 425 (2001). https://doi.org/10.1016/S1468-6996(01)00014-6

45. Y. Li, X. Chen, J. Zhou, X. Liu, D. Zhang, F. Du, W. He, P. Jia, H. Liu, Int. J. Mech. Syst. Dyn. **2**, 50 (2022). https://doi.org/10.1002/msd2.12033
46. A. Katunin, I. Pivdiablyk, L. Gornet, P. Rozycki, Compos. B **238**, 109898 (2022). https://doi.org/10.1016/j.compositesb.2022.109898
47. T. Lukács, C. Pereszlai, N. Geier, Compos. Part B **248**, 110381 (2023). https://doi.org/10.1016/j.compositesb.2022.110381
48. W.K. Tredway, United technologies research center, R95-5/102.0006-3 (1995)
49. Y.H. Huh, J.I. Kim, D.J. Kim, G.C. Lee, Trans. Korean Soc. Mech. Eng. A **36**(9), 1053 (2012). (**In Korean**)
50. K.W. Kang, Y.S. Kim, M.H. Lee, R. Choi, J. Korean Soc. Saf. **20**(4), 14 (2005). (**In Korean**)
51. J.E. Grady, E.H. Meyn, Scientific and Technical Information Division, Lewis Research Center Cleveland, NASA Technical Memorandum, Ohio, (1989).
52. D. Kreculj, B. Rašuo, Tehnicki Vjesnik **20**(3), 485 (2013)
53. V. Alagumalai, V. Shanmugam, N.K. Balasubramanian, Y. Krishnamoorthy, V. Ganesan, M. Försth, G. Sas, F. Berto, A. Chanda, O. Das, Polymers **13**, 2591 (2021). https://doi.org/10.3390/polym13162591
54. X.L. Fan, Q. Sun, M. Kikuchi, J. Solid Mech. **2**(3), 275 (2010)